Complete citation:

Hou, J., Hokmabad, B. V., & Ghaemi, S. (2017). Three-dimensional measurement of turbulent flow over a riblet surface. *Experimental Thermal and Fluid Science, 85*, 229-239. doi: 10.1016/j.expthermflusci.2017.03.006

The final publication is available at https://doi.org/10.1016/j.expthermflusci.2017.03.006

Three-dimensional measurement of turbulent flow over a riblet surface

Jianfeng Hou, Babak Vajdi Hokmabad, Sina Ghaemi*

Department of Mechanical Engineering, University of Alberta, Edmonton, Alberta T6G 2G8, Canada

Abstract

Measurement of three-dimensional (3D) turbulence over riblet surfaces is challenging due to the small size of the grooves and the requirement for measurement in the inner layer. The capability of two-dimensional (2D) and 3D particle image velocimetry (PIV) and particle tracking velocimetry (PTV) for characterization of the 3D structure of turbulent flow over a riblet surface with groove spacing of 750μm at Re_τ = 147 (based on friction velocity and half channel height) is investigated. The 2D measurements were carried out using standard planar PIV and high-magnification long-range microscopic PTV (micro-PTV). The investigated 3D techniques include tomographic PIV (tomo-PIV) and 3D-PTV. The results are evaluated in comparison with measurement over a smooth surface and also with direct numerical simulation (DNS) of channel flow by Tsukahara *et al.* [1] at Re_τ = 150. The reflection of the laser light from the smooth and riblet surfaces is significantly different in spite of the wall-parallel illumination. This resulted in biased near-wall (y/H < 0.05) measurement using planar PIV. The shortcoming was fulfilled by micro-PTV which could measure the mean velocity profile within the linear viscous sublayer ($2 < y^+ < 5$) and showed a 6.1% reduction of the skin-friction over the riblet surface. Micro-PTV also accurately measured the location of the $\langle u^2 \rangle$ peak and its magnitude reduction over the riblet surface compared with planar PIV. The Planar PIV measured $\langle v^2 \rangle$ peak which is further away from the wall at y/H = 0.15 and also the $\langle uv \rangle$ profile in the outer layer. The $\langle uv \rangle$ profile showed 7.4% reduction of wall shear stress over the riblet surface. 3D-PTV showed a 9.4% reduction of the $\langle w^2 \rangle$ peak and attenuation of v and w fluctuations over the riblet surface compared to the smooth surface through quadrant analysis. The three components of fluctuating vorticity measured by tomo-PIV showed negligible variation over the two surfaces due to the random noise and lack of spatial resolution. Quadrant analysis using planar PIV showed attenuation of the sweep and ejection events near the riblets, which indicates weaker streamwise vortices. Two-point correlation of PIV measurement also demonstrated increase of the coherence of the low and high-speed steaks over the riblets.

Keywords

Turbulent channel flow; Riblet surface; Particle image velocimetry; Particle tracking velocimetry

1. Introduction

Wall-normal momentum transport in turbulent flows causes larger skin-friction and more energy consumption in many applications including pipeline, marine, and aerospace industries. Among the methods for reduction of the skin-friction, only a few have short-term potential to be applied in practice. A riblet surface is a simple passive drag reduction (DR) technique that was inspired by the texture of the sharkskin. The surface has been replicated as microgrooves aligned in the streamwise direction [2]. Riblets are known to modify the structure of the near wall turbulence and reduce the skin-friction up to about 10% [3,4].

The performance of a riblet surface depends on the groove spacing relative to the scale of the near wall turbulence. According to Walsh and Lindemann [3], DR over riblets at different Reynolds numbers can be expressed in terms of dimensionless riblet spacing, $s^+ = s / (u_\tau / \nu)$, in which s is the lateral riblet tip spacing, ν is the kinematic viscosity, and u_τ is the friction velocity over the smooth surface exposed to the same bulk flow velocity. DR is quantified as DR = $(\tau - \tau_0) / \tau_0$ where τ is the wall shear stress over riblet surface and τ_0 is wall shear stress over the smooth surface. One of the earliest experimental works by Walsh [5] indicated that DR occurs only for $s^+ < 30$ and the maximum reduction is observed at s^+ = 15-20 for riblets with both sharp and curved shapes. Bechert et al. [4] provided a thorough set of DR measurements for riblets of various shapes and dimensions. Their results for small s^+ showed the riblet protrusion is immersed only in the viscous sublayer and the outer layer behaves the same as the flow on smooth wall [6]. This *viscous regime*

continues up to $s^+ \approx 17$ as DR monotonously increases [4]. At the optimal riblet spacing of $s^+ \approx 17$, DR reaches a maximum and the viscous regime starts to break down [4, 7]. As a consequence, DR gradually diminishes and a drag increase regime with *k*-roughness behavior forms [7].

The mechanism for DR developed by riblet surfaces has been investigated in association with the near wall coherent structures, which generate most of Reynolds stresses and consequently turbulent kinetic energy [8]. Choi et al. [9] observed that ejection and sweep motions are attenuated while the first and third quadrants are unchanged over the riblet surface. They also observed that riblets modify skin-friction through restricting the motion of streamwise vortices. Later work by Suzuki and Kasagi [10] observed that skin-friction reduction is closely related to the motion of streamwise vortices. The flow visualization studies of Lee and Lee [11] observed an upward shift of the streamwise vortices away from the wall to the region above the riblets where mean shear is smaller. These investigations also indicate that understanding the DR mechanics and development of modern riblet surfaces rely on scrutiny of the 3D structure of near-wall turbulence.

Numerical investigations have provided detailed characterization of the flow field over riblet surfaces that are difficult to obtain from experiments. For example, the DNS of Choi et al. [9], Goldstein et al. [12] and El-Samni et al. [13] have characterized high-order turbulence statistics and vorticity field over the riblets and inside the riblet valleys. However, extension of the numerical simulations to higher Reynolds number and modern riblet surfaces with micro-size, 3D or hierarchical grooves (e.g., [14] and [15]) is still limited by computational resources and flow investigations require application of advanced measurement techniques.

Measurement of near-wall turbulence is challenging due to the small-scale of the turbulence and the large velocity gradient. There are more difficulties over riblet surfaces since the sub-millimeter grooves typically affect high-order turbulence statistics and the 3D structure of vortices within the inner layer. Choi [16] investigated the near-wall turbulence over a riblet surface using hot wire anemometry (HWA). In addition to point-wise limitation, the larger heat transfer rate near the solid surface affects the accuracy of HWA. Suzuki and Kasagi [10] carried out a detailed investigation of second-order statistics of all the three components of velocity fluctuations above the riblets using 3D-PTV. However, the low-tracer density images did not allow investigation of the instantaneous turbulence structure. Lee and Lee [11] investigated the flow inside the riblet valley using planar PIV and PTV techniques. Lee and Choi [17] observed reduction of the number frequency of spanwise vortices using a high-resolution planar PIV. Therefore, previous investigations applied each measurement technique to characterize a certain feature of the complex small-scale 3D flow over riblets.

The present investigation investigates the capability of four image-based techniques including 2D-PIV, long-range micro-PTV, tomo-PIV, and 3D-PTV in resolving the near-wall turbulent structures over a riblet surface at $Re_\tau = 147$. Measurement of mean velocity in the inner layer, all components of the Reynolds stress tensor, two-point correlation, and three components of vorticity fluctuation are evaluated. The measurements are evaluated by comparing with measurements over a reference smooth surface, DNS over smooth wall channel flow by Tsukahara et al. [1] at $Re_\tau = 150$, and the previous experimental and numerical works over riblet surface.

2. Experiment setup

2.1 Flow facility

The experiments were carried out in a closed-loop, free-surface flume with a 5.2 m long and 0.68 m wide test section partially filled to a height of 0.23 m. A 2D channel flow of 3 m length (L) in the streamwise (x) direction was formed inside the flume using a bottom glass plate and an upper acrylic plate as shown in Fig. 1. The cross-section of the channel had 20 mm height (H) and 540 mm width (W), corresponding to y (wall-normal) and z (spanwise) directions, respectively. A honeycomb flow straightener was placed at the entrance to break down the large vortices and to increase the uniformity at the entrance. The bottom glass plate was kept 30 mm above the water channel bottom wall to prevent the flume boundary layer from entering the 2D-channel. This ensures formation of new boundary layers on both lower and upper walls and a symmetric profile. A 570 mm long and 320 mm wide interchangeable module was located 1.6 m ($80H$) downstream from the entrance, where the turbulent channel flow was fully developed. This module was used to introduce the different surface boundary conditions under investigation.

Instantaneous velocity components in the x, y, and z directions are specified by U, V, and W while the fluctuations are denoted by u, v, and w. The average velocity in the y direction (bulk velocity) was $U_b = 0.24$ m/s. The Reynolds number based on the full channel height is $Re_H = 4780$ with a kinematic viscosity of $\upsilon = 1.004 \times 10^{-6}$ m^2/s. The wall unit was calculated to be $\lambda_0 = 67.9$ μm with a friction velocity

of $u_{\tau 0}$ = 0.0148 m/s over the smooth wall (estimated using the PTV system as detailed in Section 3.1). Reynolds number based on friction velocity and half channel height was Re_τ = 147. The estimated wall shear and friction coefficient based on PTV are 0.22 N/m^2 and 0.0076, respectively.

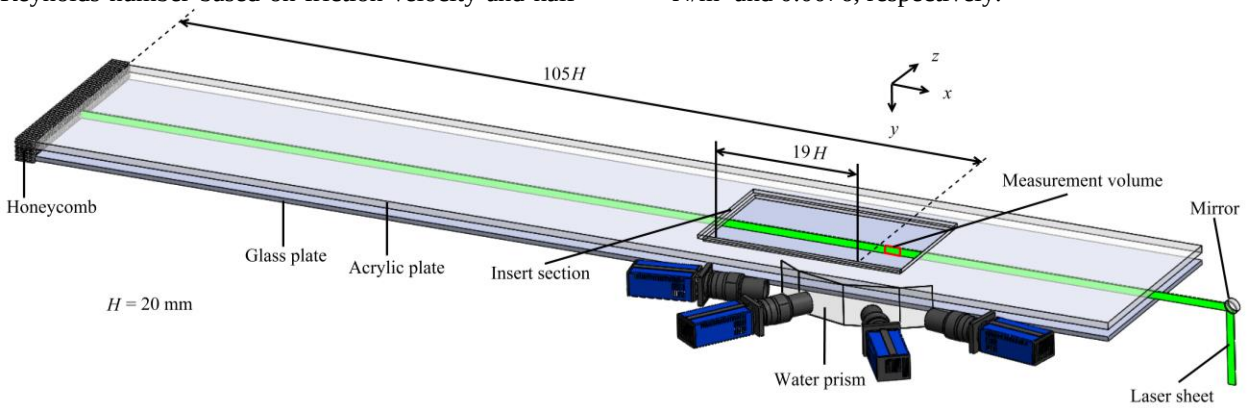

Fig. 1. A schematic of the experimental setup showing the 2D-channel, the insert module to place the riblet or smooth surface, and the tomo-PIV/3D-PTV measurement setup. The channel flow is embedded inside the large flume.

The friction coefficient for a turbulent channel flow is estimated using

$$c_f = 0.0791 \left(\frac{U_b d}{\nu}\right)^{-1/4} \quad (1)$$

according to the Blasius law for smooth pipes and ducts (Dean [18]). Here d is the equivalent hydraulic diameter defined as

$$d = \frac{4A}{P}. \quad (2)$$

where A is the cross-sectional area and P is the wetted perimeter. In the current study, d is 0.039 m. The friction coefficient, wall shear stress, and friction velocity are estimated to be c_f = 0.0081, τ = 0.23 N/m^2, u_τ = 0.0152 m/s, respectively. The theoretical estimation of c_f is about 7% different from the estimated value based on PTV measurements.

2.2 Riblet and smooth surfaces

The riblet surface consists of trapezoidal grooves with s = 750 μm, h = 375 μm, and $\alpha = 30^\circ$ as shown in Fig. 2, manufactured by CNC milling (with machine tolerance: 12.7 μm) from a cast aluminum block. The dimensions correspond to h / s = 0.5 and s^+ = 11 at the current flow conditions. The reference smooth plate was a machined aluminum surface. Both surfaces were 430 mm long, 280 mm wide, and 6.35 mm thick. The surfaces could be placed inside the interchangeable module.

The protrusion height (h_{p0}) of a riblet surface is defined as the wall-normal distance from the riblet tip to a virtual origin, defined as the wall-normal position where an imaginary smooth surface generates the same drag and the same outer layer velocity profile as the riblet surface [9,19]. The virtual origin of riblets has been evaluated by several approaches in the literature.

Perry and Joubert [27] introduced an iterative technique based on a modified version of the Clauser's method to estimate the virtual origin of rough walls (with drag increase), located between the top and the bottom of the roughness. Hooshmand et al. [20] evaluated the applicability of this method to a riblet surface (with DR) and observed an erroneous virtual origin located at the base of the riblets and consequently drag increase relative to the smooth surface. Instead, they applied an extrapolation of the velocity profile within the linear viscous sublayer over the riblet valley to find the virtual origin at $\langle U \rangle = 0$. Their extrapolation showed a virtual origin almost at the midpoint between the tip and the valley of the riblet. Choi et al. [9] used the location of the maximum streamwise velocity fluctuation ($y^+ \approx 13$) to estimate the virtual origin in their DNS study. Bechert and Bartenwerfer [21] applied conformal mapping by assuming that the riblets are embedded inside the linear viscous sublayer. They analytically estimated the virtual origins as a function of the shape and geometric height of riblets without the need for any flow measurement. Bechert et al. [4] also applied the conformal mapping method and investigated DR over riblets of various geometric parameters.

The current investigation estimates the location of virtual origin and protrusion height h_{p0} using conformal mapping to mount the riblet surface with respect to the reference smooth surface. Based on Bechert and Bartenwerfer [21], the protrusion height of the current riblet design, is $h_{p0} = 0.2s$, which is

equivalent to h_{p0} = 0.15 mm. Therefore, two fifths of the height (i.e., h_{p0} = 150 μm) of the riblet protrudes into the flow to maintain the same outer layer velocity profile for both smooth and riblet experiments [18, 19]. This estimated location will be revised later by applying Hooshmand et al. [20] method based on extrapolation of mean velocity to the zero velocity location (detailed section 3.1).

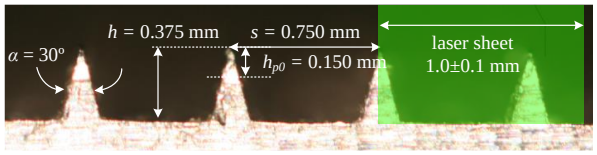

Fig. 2. An image of the cross-section of the riblet plate machined on cast aluminum.

2.3 Particle image velocimetry

PIV measurements were carried out at a magnification of M = 0.37 to cover the turbulent flow across the full channel height. The PIV system consisted of an Nd:YAG laser (Spectra-Physics, PIV400) with 532 nm wave length, maximum output of 400 mJ per pulse, and maximum repetition rate of 10 Hz. A combination of cylindrical and spherical lenses was used to reshape the laser beam into a collimated laser sheer of ~1 mm thickness. The laser sheet covered ~1.3 riblets starting from the tip of a riblet as shown in Fig 2. The collimated laser sheet was directed in the streamwise direction parallel to the channel walls by a mirror placed inside a sealed acrylic column downstream of the measurement region, as shown in Fig. 1. The wall parallel illumination reduced the glare line produced by wall reflection of the laser sheet in the PIV and PTV images. Sample PIV images of the smooth and riblet surfaces at the top wall shown in Fig. 3 (a) and (b), respectively. The test plate (smooth or riblet) is installed on the top wall while the bottom wall is always a flat surface. In spite of the wall parallel illumination, a strong glare line is observed at the smooth wall in the upper part of Fig. 3(a). In contrast, the riblet surface generated a weak glare line as shown in Fig 3(b). Scrutiny of the images also reveals mirrored particle images at the riblet wall.

Silver-coated glass spheres (Potters Industries Conduct-O-Fil® SG02S40) with 2 μm diameter and density of 4 g/cm^3 were added to the water flow as tracer particles. The tracers have a short relaxation time of τ_r = 0.7μs determined from

$$\tau_r = \frac{18\mu}{\rho_{pf} d_p^2} \qquad (3)$$

where ρ_{pf} is the density difference between the particle and the fluid, and μ is dynamic viscosity of water [38]. The estimated relaxation time of the tracers is negligible in comparison with the characteristic time scale of the fluid based on friction velocity $t^* = \nu / u_\tau^2 \approx$ 4.7 ms.

The scattered light from the tracer particles was captured by a 2048×2048 pixel (7.4 μm×7.4 μm) 14 bit double-frame CCD camera (Imager proX, LaVision GmbH) equipped with a 105 mm SLR lens at an aperture opening of f / 11. The field of view (FOV) was 40.5 mm×40.5 mm extended to 5 mm upstream of the test plate end (110H from the entrance and 20H from the beginning of the test plate). The digital resolution was 52 pixel/mm and the depth of focus (DOF) was estimated to be 3.5 mm. The Nd:YAG laser and the CCD camera were synchronized using a pulse generator (LaVision programmable timing unit) controlled by DaVis 8.2 (LaVision, GmbH). An ensemble of 10,000 pairs of double-frame images was recorded for each case with laser pulse separation of Δt = 1000 μs.

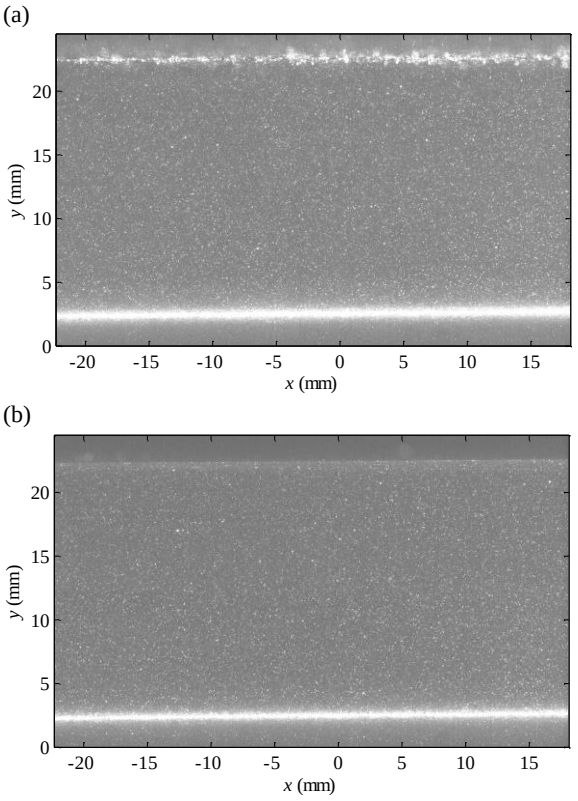

Fig. 3. Sample PIV image showing the laser reflection from (a) the smooth surface at the top and, (b) the riblet surface installed at the top wall. The bottom is a flat surface in both images. Stronger reflection at the bottom wall is associated with gradual accumulation of particles during the image acquisition.

The signal-to-noise ratio of the images was improved by subtracting the minimum intensity of the ensemble from individual images, followed by normalizing each image using the average of the ensemble. The images were processed with the ensemble of the correlation method (EC method) [23] to obtain the mean velocity profile with high spatial resolution. The final window size in the EC method was 16×16 pixels (0.31 mm×0.31 mm, 0.015H×0.015H, 4.5λ×4.5λ) with 75% overlap. A standard double-frame cross-correlation was also applied to obtain instantaneous velocity vectors and turbulence statistics. Multi-pass cross-correlation was performed for each double-frame image with final interrogation window of 48×48 pixels (0.92 mm×0.92 mm, 0.046H×0.046H, 13.5λ×13.5λ) and 75% overlap. Vector fields were post processed by applying an allowable vector range for both the streamwise (0 to 18 pixels) and the wall-normal (-3 to 3 pixels) velocity components, and also using the universal outlier detection [24]. All the processes were executed in DaVis 8.2 (LaVision GmbH). A summary of measurement parameters is available in Table 1.

2.4 Long-range micro-PTV

PTV at magnification of M = 1.84 was applied for high spatial-resolution measurements in the near wall region. The same laser, camera, timing unit, and tracer particles as those in the PIV measurement were applied. The camera was equipped with a long-range 12× microscope zoom lens (Navitar) to obtain a FOV of 8.2 mm×8.2 mm with a digital resolution of 248 pixel/mm. The numerical aperture (NA) was estimated to be ~0.025 based on the magnification from the zoom lens performance datasheet [25]. The DOF was approximately 1.02 mm [26]. An ensemble of 15,000 double-frame image pairs was acquired with Δt = 190 μs. The images were improved by subtracting minimum intensity of the ensemble from individual images and normalizing each image by the average of the ensemble. In order to eliminate any peak locking effect, a 3×3 pixel Gaussian smoothing filter was applied.

Custom processing software was developed in MATLAB (MathWorks Inc.) to detect particle pairs and obtain the velocity of individual particles based on their displacements. The algorithm first detects particles with intensity beyond a preliminary intensity of 100 counts followed by detection of local maxima within a kernel of 21 pixels [39]. The analysis of Kähler et al. [27] showed that particles smaller than 3 pixels cause peak locking and result in biased error. Also, relatively large particles were typically aspherical due to astigmatism or out-of-focus effects. Therefore, an area filter was used to select particle pairs with 3-7 pixels in diameter. Further particle selection was applied using ratios of the particles area (0.8-1.2), major over minor axis (0.7-1.3), and peak intensity (0.3-1.8) in the two image frames to reject erroneous particles and reduce peak detection errors. A Gaussian filter with a kernel of 7×7 pixels was applied to the selected particles for peak detection with sub-pixel accuracy.

A mean velocity field, obtained by applying the EC method [23] on PTV images with window size of 16×16 pixels and 75% overlap, was used as a predictor for detection of particle pairs within a search radius of 5 pixels. The vector field was post processed by limiting the wall normal velocity fluctuation to be smaller than 20% of the streamwise counterparts. Finally, the results were averaged over windows of 1910×8 pixels (7650 μm×32 μm, 0.38H×0.0016H, 112λ×0.47λ) in the x and y directions to obtain the mean velocity profile with high wall-normal spatial resolution. Turbulence intensity was obtained from larger windows of 1910×36 pixels (7.65 mm×0.145 mm, 0.38H×0.007H, 112λ×2.1λ) to ensure statistical convergence. Table 1 summarizes the measurement details.

2.5 Tomographic particle image velocimetry

Tomo-PIV can measure the three velocity components of the flow field in a volumetric domain illuminated by an expanded laser sheet. The technique is suitable for characterization of 3D structures of turbulence and in particular the 3D vorticity field since the data is obtained on a structured grid. The same laser and a set of 4 cameras of the same type as the PIV system were used for the tomo-PIV. The collimated laser sheet was expanded to 3 mm in the spanwise direction. The four cameras imaged the FOV at different angles through a prism filled with water. The prism had four glass windows ensuring each window was parallel to the front surface of a camera lens as shown in Fig. 1. The solid angle between the two outer cameras was set to 80° while the angle between the inner cameras was set to 35°. The cameras were equipped with Scheimpflug adapters and a 105 mm SLR lens at aperture setting of f / 16. Magnification and digital resolution were 0.31 and 42.9 voxel/mm, respectively. Measurement volume was 39×20×2.7 mm^3 (1674×859×117 voxel) in the x, y, and z directions, respectively. The flume was seeded with ~12 particles/mm^3, which is equivalent to particle density of 0.02 ppp. The initial mapping function for the tomographic system was carried out using the pin-hole model applied to the images of a 2D target with 0.3 mm dots spaced 2 mm apart in x-y plane. The target was traversed in the z

direction with steps of 1 mm. Root-mean-square (rms) of the pointing accuracy disparity was reduced by volume-self-calibration technique from an initial value of 1-2 pixels to less than 0.06 pixels in the domain of interest [28]. An ensemble of 4,000 double frame images has been collected for each case with Δt = 1200 μs.

Signal-to-noise ratio of the images was improved by subtracting minimum intensity of the whole set from individual images followed by normalization using the average of the ensemble. Image quality was further improved using local minimum subtraction with a kernel of 3 pixels, normalization of the intensity using a local average over a kernel of 300 pixels, and a 3×3 pixel Gaussian filter to reduce the peak-locking effect. Finally, a constant value of 20 counts was subtracted from the images to decrease the background noise level. 3D locations of the particles in 1,000 double-frame images were reconstructed using the multiplicative algebraic reconstruction technique (MART). The reconstruction volume was 45×27×7 mm^3 (1674×859×117 voxel) in the *x*, *y*, and *z* coordinates, respectively. The light intensity distribution across the spanwise depth of the reconstructed volume was used to evaluate the quality of reconstructions. The ratio of the light intensity within the illuminated region to the light intensity outside of the reconstruction was ~3. This relatively high signal to noise ratio is associated with subtraction of 20 counts from the image before the 3D intensity reconstruction process. The spanwise depth of the illuminated volume based on the reconstructed light intensity was ~2.7 mm, compatible with the thickness of the laser sheet. The standard deviation of the divergence of the velocity field ($\nabla\cdot\ \vec{V}$) is estimated to be 0.04 voxel/voxel. The quantity has been used as an indication of the accuracy of the 3D velocity field for incompressible flows [29]. Scarano and Poelma [29] also indicated 0.04 voxel/voxel for tomo-PIV measurement in a transitional cylinder wake. Multi-pass volumetric cross correlation was performed with the final interrogation volumes of 40×40×40 voxel (0.93×0.93×0.93 mm^3, 0.047*H*×0.047*H*×0.047*H*, 13.7λ×13.7λ×13.7λ) with 75% overlap. Universal outlier detection was used as a post processing step for vector fields [24]. Measurement specifications can be found in Table 1.

2.6 Three-dimensional particle tracking velocimetry

3D-PTV was applied as an alternative to tomo-PIV to obtain the three velocity components with higher spatial-resolution since this technique is not limited to the relatively large interrogation volumes. However, the drawback of the 3D-PTV relative to tomo-PIV is the unstructured instantaneous data which makes the estimation of spatial-gradient challenging. The applied 3D-PTV algorithm (DaVis 8.2, LaVision GmbH) detects and tracks particles based on triangulation of particle positions [28]. The algorithm was applied to the same 4,000 double-frame images recorded by tomo-PIV system using the same mapping function and self-calibration. The number of detected particles and the noise level were controlled using the particle intensity threshold and the allowed triangulation error. The optimum setting for statistical convergence and accuracy was maximum triangulation error of 1 pixel and a particle intensity threshold of 300 counts. The detected particle velocities were averaged over bins of 1760×20×12 pixels (41×0.47×0.28 mm^3, 2.0*H*×0.0235*H*×0.014*H*, 600λ×7.0λ×4.1λ) in the *x*, *y* and *z* direction, respectively. Table 1 summarizes the specifications of the measurement system.

Table 1. Specification of the measurement systems. The dimensions with superscript $^+$ are normalized using wall unit λ = 7.9 μm over the smooth surface.

	PIV	Planar PTV	Tomo-PIV	3D-PTV
Ensemble	10,000	15,000	1,000	4,000
Magnification	0.37	1.84	0.31	
Digital resolution	52 pix mm^{-1}	248 pix mm^{-1}	42.9 pix mm^{-1}	
Time interval Δt	1000 μs	190 μs	1200 μs	

Measurement field	2023×1224 pix 40.5×23.5 mm^2 596$^+$×346$^+$		2048×2048 pix 8.2×8.2 mm^2 121$^+$×121$^+$		1674×859×117 vox 39×20×2.7 mm^3 574$^+$×294$^+$×39.7$^+$	1760×859×117 vox 41×20×2.7 mm^3 603$^+$×294$^+$×39.7$^+$
Velocity vector	Individual correlation	Ensemble of correlations	Averaged vector field		Individual correlation	Averaged vector field
Interrogation region (IR) (Δx, Δy, Δz)	48×48 pix 0.92×0.92 mm^2 13.5$^+$×13.5$^+$	16×16 pix 0.31×0.31 mm^2 4.5$^+$×4.5$^+$	1910×8 pix 7650×32 μm^2 112$^+$×0.47$^+$	1910×36 pix 7.65×0.145 mm^2 112$^+$×2.1$^+$	40×40×40 vox 0.93×0.93×0.93 mm^3 13.7$^+$×13.7$^+$×13.7$^+$	1760×20×12 vox 41×0.47×0.28 mm^3 600$^+$×7.0$^+$×4.1$^+$
IR overlap	75%		0%		75%	0%
Vectors per field	168×102	505×306	256	56	167×85×11	42×9

3. Results and discussion

In this investigation, each measurement technique is applied to obtain specific flow statistics based on the potential of the measurement technique. Planar PIV is used to obtain mean velocity, normal and shear Reynolds stresses in the *x*-*y* plane, spanwise vorticity fluctuation, and spatial correlation of *u* and *v* components. Micro-PTV is applied to measure the mean velocity and Reynolds stresses within the inner layer ($y^+ < 50$). Spanwise Reynolds stress ($\langle w^2 \rangle$) was obtained using 3D-PTV while tomo-PIV was applied to estimate the three components of vorticity fluctuations. The top wall ($y / H = 0$) corresponds to the riblet or the smooth surface while the bottom wall at $y / H = 1.0$ always holds a smooth wall. The reference of the coordinate system ($y = 0$) for the riblet surface is at the estimated virtual origin. DNS of turbulent channel flow over a smooth wall at $Re_\tau = 150$ by Tsukahara et al. [1] is also provided as a reference for comparison.

3.1 Mean velocity profile

The profiles of mean streamwise velocity, $\langle U \rangle$ normalized by the bulk velocity U_b (average velocity along *y* direction) measured using PIV (EC method) are shown in Fig. 4. The velocity profiles of both surfaces (smooth and riblet) overlap across the bottom section of the channel ($y / H > 0.5$) where the smooth wall is installed. The velocity over the riblet surfaces is slightly larger in the top half of the channel ($0.1 < y / H < 0.5$), which is an indication of smaller skin-friction on the riblet. Although the EC method provides higher spatial resolution relative to standard PIV, the first four measurements points in Figure 4 ($y / H < 0.05$) are erroneous over the riblet surface due to the presence of mirrored particle images in the near-wall interrogation windows. Such an error is not observed over the smooth surface as the stronger wall-reflection biases the cross-correlation peak towards zero. This shortcoming in near-wall velocity measurement can be overcome by applying the PTV technique.

The velocity profiles over the smooth and riblet surface measured using micro-PTV and normalized with the corresponding friction velocity are shown in Fig. 5. The distance from the riblet tip is shown as y_t^+ in this figure. The linear fit obtained using five data points over the smooth wall in the range of $2 < y^+ < 5$ in the viscous sublayer approaches zero velocity at $y^+ = 0$ as expected for a no-slip boundary condition. The estimated friction velocity and wall unit based on the velocity gradient are $u_{\tau 0} = 0.0148$ m/s and $\lambda_0 = 67.9$ μm over the smooth surface. The intercept of the mean velocity over the riblet surface with $U^+ = 0$ is at $y_t^+ = -1.8$ (0.12 mm from the riblet tip), which is 20% different from the estimated protrusion height (0.15 mm). The estimated friction velocity and wall-unit over the riblet surface using five PTV data points in the range of $2 < y^+ < 5$ is $u_{\tau r} = 0.0139$ m/s and $\lambda_r = 72.3$ μm, respectively.

The slope of mean velocity profile ($\partial \langle U \rangle / \partial y$) in the linear viscous sublayer and consequently the wall

shear stress (τ_w) is reduced by 6.1% over the riblet surface. The same method has been used to estimate friction velocity over riblet surface by Park and Wallace [30] using HWA data and by Roggenkamp et al. [31] based on micro-PTV measurement. The estimated DR based on $\partial\langle U\rangle/\partial y$ agrees with direct force measurement of Bechert et al. [4] showing about 6% DR over riblets at s^+ = 11 between Re_H = 10000 ~ 33000.

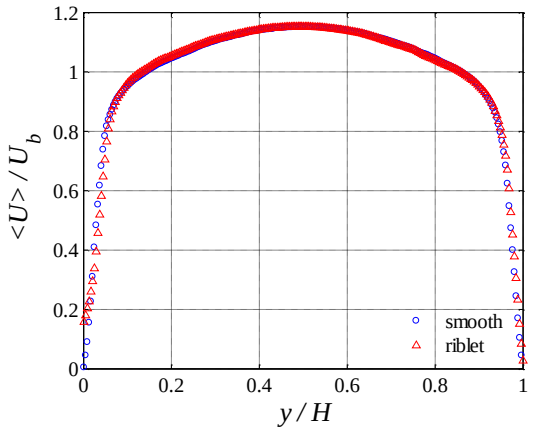

Fig. 4. Normalized velocity with U_b from PIV measurement processed using ensemble of correlation method with 16 × 16 window size and 75% overlap.

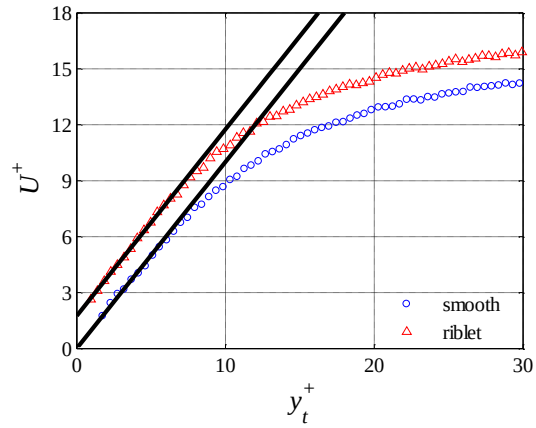

Fig. 5. Velocity profile measured using long range microscopic PTV normalized by the friction velocity of the corresponding surface. The axis label y^+_t is the wall normal distance with respect to the tip of the riblet.

The uncertainty in the estimated wall shear stress using the $\partial\langle U\rangle/\partial y$ slope depends on the uncertainty of mean velocity (ε_U) and wall location (ε_y) obtained from micro-PTV velocity data and raw images, respectively. For simplicity of the uncertainity estimation, it is assumed that the slope is calculated using two data points: $\langle U\rangle$ measured at y^+ = 5 and $\langle U\rangle$ (assumed to be zero) at the detected wall location. Therefore, this is an overestimation of the possible uncertainty and should be considered as an upper bound on the error. Therefore, the wall-shear stress can be estimated from

$$\tau_w = \mu \frac{\langle U\rangle_{|y^+=5} \pm \varepsilon_U}{5\lambda \pm \varepsilon_y} \tag{3}$$

The PTV uncertainty is assumed to be ε_U = 0.1 pix (0.0021 m/s, $0.14u_{\tau 0}$) based on the accuracy of particle peak detection [26]. The wall location has been estimated by finding the mid-location between the near wall particles and their mirrored image with an uncertainty of ε_U = 0.5 pix. Since $\langle U\rangle$ at y^+ = 5 is $5u_{\tau 0}$ according to the law of the wall and $\varepsilon_U = 0.11u_\tau$, Equation 3 can be rewritten as

$$\tau_w = \mu \frac{5u_{\tau 0} \pm 0.14u_{\tau 0}}{5\lambda_0 \pm 0.03\lambda_0} \tag{4}$$

Applying $\lambda_0 = \nu / u_\tau$, the equation can be simplified to

$$\tau_w = \rho u_{\tau 0}^2 (1 \pm 0.03) \tag{5}$$

This estimated uncertainty is based on the minimum and maximum values of Equation 4, which results in ±3% error in τ_w. However, this is an upper bound on the uncertainty as only one data point at y^+ = 5 is applied to obtain the linear fit. The additional data points at $y^+ < 5$ are expected to considerably reduce the uncertainty of the fitted line.

A semilog plot of mean velocity versus the wall-normal distance normalized by inner scaling of the corresponding surface is shown in Fig. 6. In the linear viscous sublayer, both velocity profiles follow the law of the wall $y^+ = u^+$. The data of the smooth wall overlaps with the logarithmic law with κ = 2.5 and B = 5.5 indicating fully developed state of the flow. The slope of the log law (κ) over the riblet wall is the same as that of the smooth wall. However, the intercept (B) over the riblet surface is larger and equal to 7.2. An upward shift of the log-law and a thicker viscous sublayer has been observed by Hooshmand et al. [20], Choi et al. [9] and Lee and Choi [17] over riblet surfaces. The thicker viscous sublayer shows that the intense turbulent motions of the buffer layer are further away from the wall surface. This attenuates diffusivity of turbulence in the immediate vicinity of the wall, and consequently reduces $\partial\langle U\rangle/\partial y$ and skin-friction. Thicker viscous sublayer is also an indication of larger viscous dissipation by the smallest eddies [30]. Therefore, the log layer, which represents the balance of production of turbulence and viscous dissipation [34], is shifted upward away from the wall as observed in Fig 6.

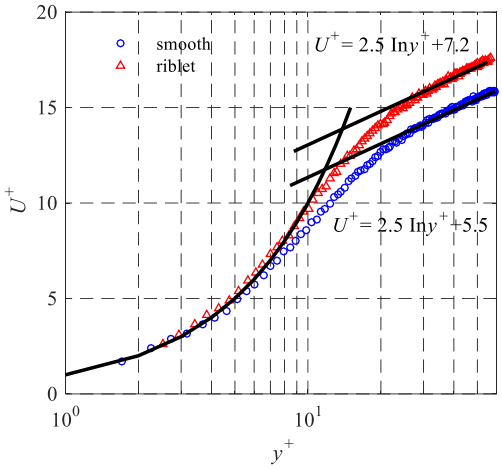

Fig. 6. A semi-logarithmic plot of mean velocity obtained from long-range micro-PTV. The data over each surface is normalized using the corresponding inner scaling.

3.2 Turbulence intensities

The streamwise velocity fluctuation from PIV is shown in Fig. 7. The overlap of the near-wall interrogation windows with the glare of the laser light at the wall and the mirror image of the particles results in a biased error in the first few near-wall vectors ($y / H < 0.03$). As a result, $\langle u^2 \rangle$ monotonically increases over the smooth wall and the $\langle u^2 \rangle$ peak is not observed. However, the riblet surface has a smaller wall reflection, which results in reduction of $\langle u^2 \rangle$ toward the wall and appearance of $\langle u^2 \rangle$ peak over the riblet surface. Away from the wall, $\langle u^2 \rangle$ profile of the smooth surface agrees well with the DNS. The $\langle u^2 \rangle$ intensities over the bottom wall ($y / H > 0.5$) for the two cases overlap. In the top half of the channel ($y / H < 0.5$), $\langle u^2 \rangle$ is slightly smaller over the riblet wall.

The near-wall measurement of $\langle u^2 \rangle$ with higher spatial-resolution is available from PTV in Fig. 8. In contrast to PIV, near-wall turbulence measurement by PTV is not significantly affected by wall reflection or mirrored particle images and the $\langle u^2 \rangle$ peak is captured over both surfaces. Normalized $\langle u^2 \rangle$ peak is ~8.1 and located at $y^+ = 13$ over the smooth wall. The peak value is ~12% larger than that of the DNS of Tsukahara et al. [1], which has normalized peak value of 7.2. The discrepancy is associated with random noise of the PTV process, which is expected to be present in both smooth and riblet data. The PTV results show 5.9% reduction of the $\langle u^2 \rangle$ peak and a slight shift of the peak away from the wall to $y^+ = 15$ over the riblet surface. This shift of the $\langle u^2 \rangle$ peak agrees with the thicker viscous sublayer observed based on the semi-log plot of Fig 6. Suzuki and Kasagi [10] observed about ~7% reduction in $\langle u^2 \rangle$ peak value using 3D-PTV measurement while the HWA of Choi et al. [9] showed about ~13% reduction.

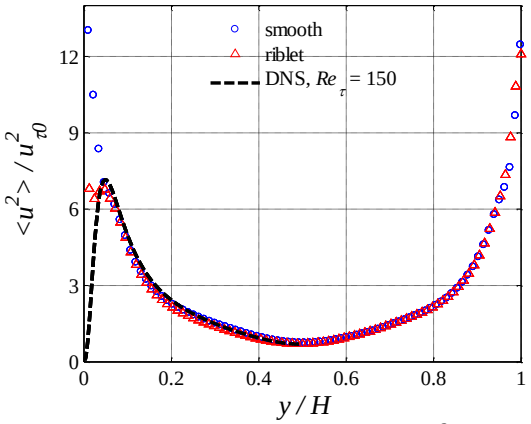

Fig. 7. Streamwise velocity fluctuation ($\langle u^2 \rangle$) from PIV measurement normalized using $u_{\tau 0}$ of the smooth wall.

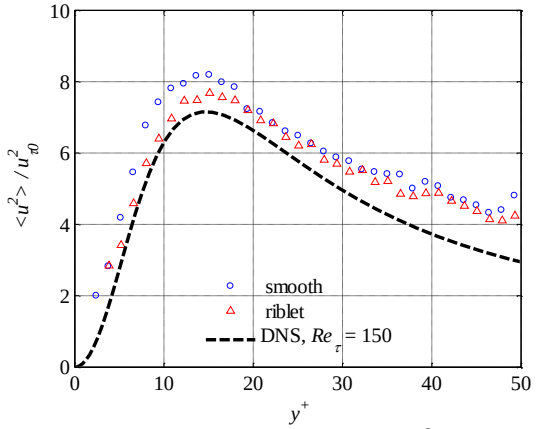

Fig. 8. Streamwise velocity fluctuation ($\langle u^2 \rangle$) from planar PTV measurement normalized using $u_{\tau 0}$ of the smooth wall.

The normalized wall-normal velocity fluctuation from PIV results are shown in Fig. 9. The peak value of $\langle v^2 \rangle$ over the smooth surface is larger than that of DNS and is located at about $y / H = 0.15$ ($y^+ = 47$). The discrepancy slightly reduces towards the channel centerline. The largest discrepancy occurs at about $y / H = 0.15$ and is equivalent 0.005 m/s or 0.24 pixels (estimated using digital resolution and pulse separation time). The profile for the smooth case is symmetric with less than 2% difference in peak value over top and bottom walls. The $\langle v^2 \rangle$ peak over the riblet wall reduces by 9.4% and the peak location is shifted away from the wall to $y^+ = 49$ relative to that of the smooth wall. Note that the difference between the peaks near the bottom wall ($y / H = 1$) could be associated with the large $\langle v^2 \rangle$ reduction on the top wall and consequently asymmetry of the channel flow. The local minimum of $\langle v^2 \rangle$ at the mid-section

of the channel is also slightly moved towards the riblet wall and is located at $y / H = 0.48$.

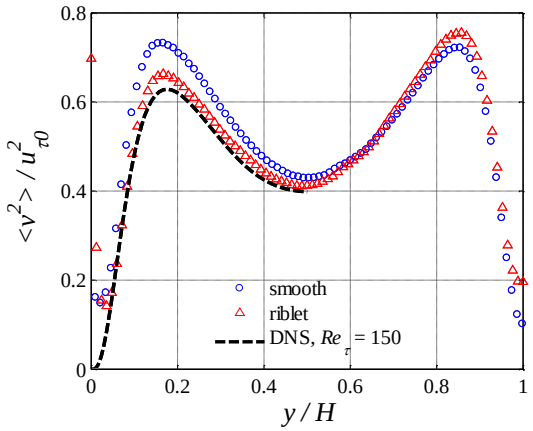

Fig. 9. Wall-normal velocity fluctuation ($<v^2>$) from PIV measurement normalized using $u_{\tau 0}$ of the smooth wall.

3D-PTV is applied to measure the spanwise velocity fluctuation due to its higher spatial resolution relative to tomo-PIV. The 3D-PTV measurements in Fig. 10 show a symmetric profile over the smooth surface that overlaps with the riblet data at $y / H > 0.5$. The measured $<w^2>$ is higher relative to the DNS, with the largest error estimated to be about 0.34 pixels. The peak location from the 3D-PTV is at $y / H = 0.1$ (equivalent to $y^+ = 31$) which is slightly different from $<w^2>$ peak of DNS. The peak value is reduced by 9.4% over the riblet surface according to the 3D-PTV measurement. The DNS of Choi et al. [9] and the 3D-PTV of Suzuki and Kasagi [10] have recorded reductions of the three components of velocity fluctuations over riblets. Choi et al. [9] recorded 5%, 10% and 10%, reduction of $<u^2>$, $<v^2>$ and $<w^2>$, respectively. The peaks of all components of turbulence intensities over the smooth wall of current study at $Re_\tau = 147$ measured using microscopic and 3D-PTV are higher compared to the DNS of Tsukahara et al. [1] at $Re_\tau = 150$. The discrepancy is associated with the measurement noise of PTV and also small vibration of water channel facility due to pump operation.

The measurements showed a reduction of all three turbulent fluctuations in the near wall region of the riblets. The reduction of $<u^2>$ and $<v^2>$ is an indication of weaker ejection and sweep motions which are the main mechanisms of turbulence production in wall-turbulence [32]. This is in agreement with the reduction of Reynolds shear stress $<uv>$, indicating smaller production of turbulence kinetic energy. The ejection and sweep motions are generated by quasi-streamwise and spanwise vortices. The attenuation of $<w^2>$ is associated with weaker quasi-streamwise vortices. Characterization of the ejection/sweep motions and the vortical structures is scrutinized in the next sections.

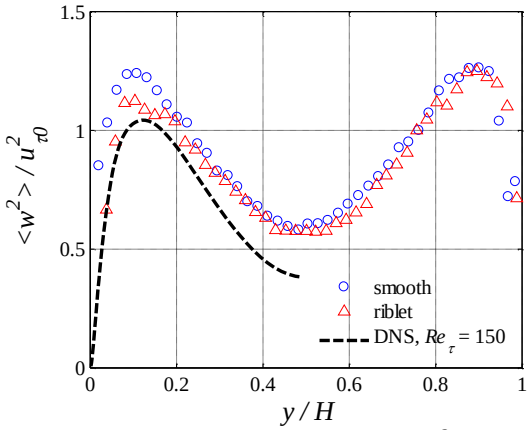

Fig. 10. Spanwise velocity fluctuation ($<w^2>$) from 3D-PTV measurement normalized using $u_{\tau 0}$ of the smooth wall.

The normalized Reynolds shear stress from the PIV measurements is presented in Fig. 11. The intercept of the linear fit on the data within $0.2 < y / H < 0.5$ (the linear range) with $y / H = 0$ is used to estimate the wall shear stress following

$$\tau_w = 0.5H \times \rho \frac{\langle uv \rangle_{y=0.5H} - \langle uv \rangle_{y=0.2H}}{0.3H} \qquad (6)$$

The presence of a linear section of the $<uv>$ profile also indicates fully developed state of the second-order statistics, i.e., statistics are independent of $\partial/\partial x$. The results show 7.4% reduction of wall shear stress over the riblet surface, which is in good agreement with the 6% reduction observed by Bechert et al. [4] and also the 6.1% reduction estimated using the slope of the linear viscous sublayer in Fig. 5. The peak values of $<uv>$ has also reduced by 11%, which indicates reduction of turbulence production. Choi et al. [9] reported a 12% reduction and Suzuki and Kasagi [10] observed 15% reduction of the peak value over riblet surfaces.

The uncertainty in Equation 6 can be estimated using the $<uv>$ error and the error in locating the mid-channel. The error in measurement of $<uv>$ is $\varepsilon_{uv} = 0.2u_{\tau 0}^2$ assuming 0.1 pix uncertainty in the instantaneous velocity. An error of $\varepsilon_y = 0.5$ pix $= 0.03\lambda_0$ is also considered in locating the middle of the channel. The equation for estimation of wall shear stress with the uncertainty values becomes

$$\tau_w = \rho u_{\tau 0}^2 \left(1 \pm \frac{\varepsilon_{uv}}{0.6u_{\tau 0}^2}\right)\left(1 \pm \frac{\varepsilon_y}{0.5H}\right) \qquad (7)$$

This equation can be simplified to

$$\tau_w = \rho u_{\tau 0}^2 (1 \pm 0.03). \quad (8)$$

The estimated uncertainty is 3%, which is similar to the uncertainty based on the $\partial\langle U\rangle/\partial y$ method. This is also an overestimation of the uncertainty as only one $\langle uv\rangle$ data point is applied (assuming $\langle uv\rangle = 0$ at $y = 0.5H$ is given). The actual uncertainty is expected to be smaller since several data points between $0.2 < y/H < 0.5$ are applied to obtain the slope in Figure 11.

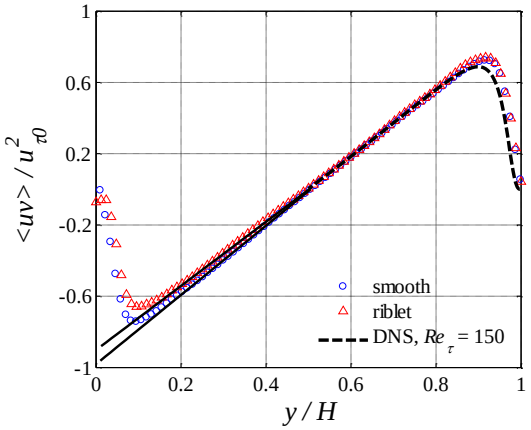

Fig. 11. Reynolds shear stress ($\langle uv\rangle$) from PIV measurement normalized using $u_{\tau 0}$ of the smooth wall. The solid lines show linear fit over the data with the range of $0.2 < y/H < 0.5$. The DNS data is only shown at lower half of the channel (i.e., $y/H > 0.5$) for clarity.

3.3 Quadrant analysis

The riblet surface changes the rate of energy transfer in the near wall region [32]. Quadrant analysis provides detailed information on the magnitude, direction, and correlation of u and v fluctuations, and therefore their contribution to turbulence production [33]. The four quadrants are defined as Q1 ($u > 0$ and $v > 0$), Q2 ($u < 0$ and $v > 0$), Q3 ($u < 0$ and $v < 0$) and Q4 ($u > 0$ and $v < 0$). Q2 and Q4 are known as ejection and sweep motions, respectively, due to their significance in turbulence production. Reynolds shear stress is conditionally averaged based on the quadrant of the fluctuations using

$$uv_{con} = \langle uv\rangle|_{Q1,\ Q2,\ Q3,Q4}. \quad (8)$$

The conditional averaged Reynolds shear stress from PIV normalized using the smooth wall friction velocity is given in Fig. 12. Sweep events in Q4 dominate the turbulence production near the wall till $y/H \approx 0.06$ ($y^+ = 16$) where the magnitude of sweep and ejection events reaches the same level. This is in accordance with the observation of Wallace et al. [34] that the sweep and ejection have the same contribution to the Reynolds shear stress at $y^+ \sim 15$. Beyond this point, the ejection events have a larger contribution to the total wall shear stress in agreement with Kim et al. [35]. The first and third events make a small negative contribution to turbulence production. All four events are slightly attenuated over the riblet surface. The reduction of ejection and sweep events over the riblet surface is associated with the dampened strength of the streamwise vortices at the near-wall region [8, 9]. All four events have been shifted slightly away from the wall in the riblet case. The suppression of the sweep and ejection events has also been observed by Choi et al. [9] and Sasamori et al. [15].

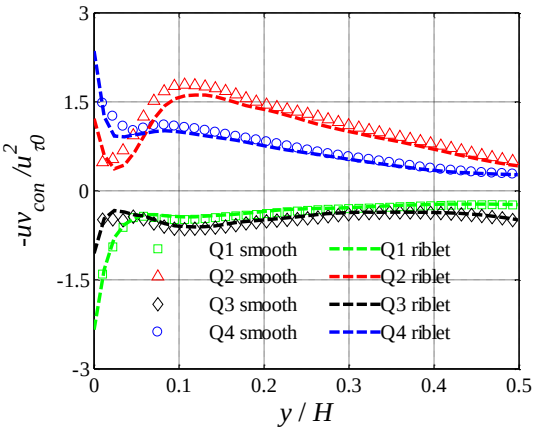

Fig. 12. Amplitude of each quadrant of Reynolds shear stress from PIV measurement normalized using $u_{\tau 0}$ of the smooth wall.

Quasi-streamwise vortices in the near-wall region are associated with v and w fluctuations. The strength of the streamwise vortices over riblet surfaces can be investigated by quadrant distribution of v and w fluctuations as shown in Fig. 13 obtained from 3D-PTV for $y^+ = 6$. The distribution of v and w is symmetric with respect to zero axis. The area of 0.5% contour is considerably reduced over the riblet surface in all quadrants indicating absence of strong v and w fluctuations over the riblet surface. This observation supports dampened motion of streamwise vortices over riblet surfaces.

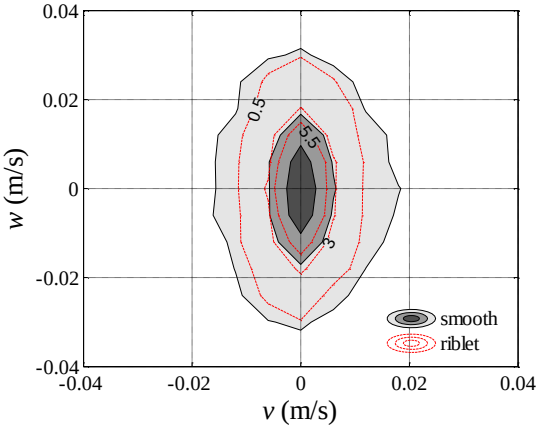

Fig. 13. Probability density function of wall-normal (v) and spanwise (w) velocity fluctuation from 3D-PTV measurement at $y^+ \approx 6$. The filled contours in dark gray, medium gray and light gray, along with the red dash-line contours from inner circle to outer circle denote 5.5%, 3.0% and 0.5% probability density function values, respectively.

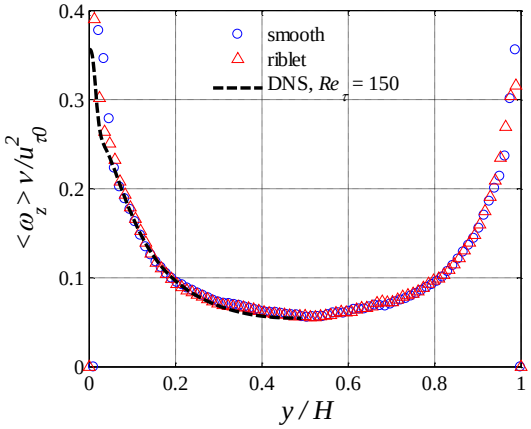

Fig. 14. Spanwise root mean square vorticity fluctuation from PIV measurement normalized using $u_{\tau 0}$ of the smooth wall.

3.4 Vorticity

The normalized root-mean-square of vorticity fluctuation is defined as

$$\omega_i^+ = \sqrt{<\omega_i^2>}\nu / u_{\tau 0}^2 \qquad (9)$$

Here, i refers to the vorticity components (i.e., ω_x, ω_y, and ω_z). The PIV measurement of spanwise vorticity fluctuation, ω_z^+, agrees with the DNS data as shown in Fig. 14. A first order central difference scheme is applied to calculate the velocity gradients. It is observed that ω_z^+ is slightly smaller over the riblet surface up to y/H = 0.05 (equivalent to y^+ = 15). Beyond this point, ω_z^+ has the same magnitude over the smooth and riblet surfaces. This trend agrees with the result of Sasamori et al. (2014).

Tomo-PIV measurement can be used to obtain the three ω_x^+, ω_y^+, and ω_z^+ components. In order to calculate the velocity gradient from tomo-PIV data, a second order regression was applied to reduce the measurement noise [36]. The function

$$f_{reg}(r_x,r_y,r_z) = a_0 + a_1 r_x + a_2 r_y + a_3 r_z + a_4 r_x r_y + a_5 r_x r_z + a_6 r_y r_z + a_7 r_x^2 + a_8 r_y^2 + a_9 r_z^2 \qquad (10)$$

is fit to each velocity fluctuation component in a 5×5×1 neighborhood of a point x_0, y_0, z_0, where r_x, r_y, r_z are the relative distances in the x, y and z direction, respectively. The coefficients a_i are the fitting parameters which are obtained using a least-mean-square method. The coefficients a_1, a_2, a_3 are the local gradients of velocity fluctuations in the x, y and z direction, respectively [36]. Due to the limited number of data, kernel size of 1 was taken in the z direction.

Fig. 15 shows the vorticity fluctuations from the tomo-PIV results. A negligible difference is observed between the smooth and riblet surfaces. In the midsection of the channel, all three vorticity components should overlap as the DNS data shows. However, the tomo-PIV data show larger values for all components and in particular for ω_x^+ and ω_y^+, due to the higher measurement noise of the out-of-plane velocity components. Worth et al. [37] simulated the measurements of tomo-PIV and showed at least 45% measurement uncertainty related to the velocity gradient fields. Choi et al. [9] numerically showed a marginal reduction for vorticity fluctuations on the riblet wall. El-Samni et al. [13], on the contrary, reported an increase of ω_y^+ and ω_z^+ in the range of $20 < y^+ < 75$ over the riblets.

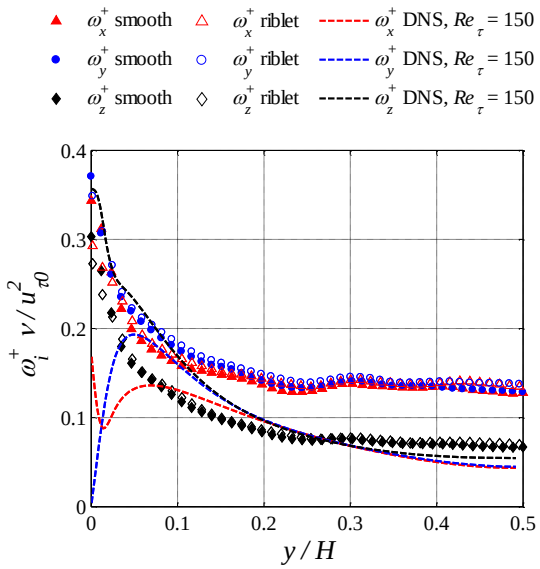

Fig. 15. Root mean square vorticity fluctuations from tomo-PIV measurement with $u_{\tau 0}$ over smooth wall.

3.5 Length-scale of turbulent structures

Spatial correlation of velocity components can demonstrate the average length scale of the turbulent structures. The streamwise spatial correlation of a one-dimensional row of *u* fluctuations from PIV data is defined as

$$C'_{uu}(\delta x^+)=\frac{<u(x,y_0)u(x+\delta x,y_0)>}{<u(x,y_0)^2>} \qquad (11)$$

and for *v* fluctuations as

$$C'_{vv}(\delta x^+)=\frac{<v(x,y_0)v(x+\delta x,y_0)>}{<v(x,y_0)^2>}, \qquad (12)$$

respectively. Here δx^+ is the streamwise shift of the one dimensional row of PIV data located at wall-normal position of y_0. Streamwise C_{uu} (δx^+) and C_{vv} (δx^+) resolved from PIV measurements are shown in Fig. 16. At y^+ = 11, C_{uu} (δx^+) over the riblet decays slower than that of the smooth wall, indicating longer low and high speed streaks in the streamwise direction. In polymer DR study by White et al. [38], the streaks are shown to be more organized in the DR case which supports the observed change in C_{uu} (δx^+). In comparison, C_{vv} (δx^+) decreases above the riblet wall, showing a shorter wall-normal extent of the ejection and sweep motions over the riblets. Suzuki and Kasagi [10] noticed a reduction of C_{vv} (δx^+) but observed no change of C_{uu} (δx^+). Away from the riblets at y^+ of about 25, C_{uu} (δx^+) and C_{vv} (δx^+) overlap over both surfaces as it is expected in the outer layer.

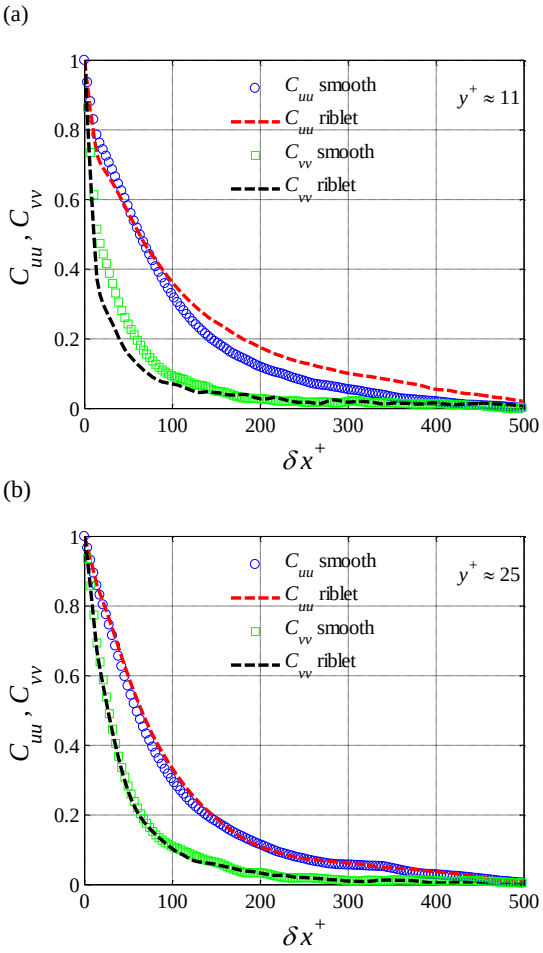

Fig. 16. Two-point correlation in streamwise direction (a) $y^+ \approx 11$ (b) $y^+ \approx 25$ from 2D-PIV data.

4. Conclusion

The performance of planar PIV, long-range micro-PIV, 3D-PTV, and tomo-PIV in characterization of the turbulent flow over a riblet surface is evaluated by comparison with measurement over the smooth wall and also DNS at same Reynold number by Tsukahara *et al.* [1]. PIV and PTV images of the smooth wall show a stronger glare line due to the reflection of the laser sheet in spite of the wall-parallel illumination. The glare line is weaker over the riblet surface possibly due to riblet cavities. Mirrored images of the tracer particles are also observed in images of the riblet surface. As a result, PIV is not suitable for characterization of the near wall flow (y/H < 0.05) since the near wall interrogation windows (at least 4) are strongly

affected by the extent of the glare line. The mean velocity measured by PIV in the vicinity of the riblet surface is overestimated. The profile of $\langle u^2 \rangle$ also monotonically increases towards the wall and $\langle u^2 \rangle$ peak is not captured in the PIV measurement. Although PIV could measure the $\langle v^2 \rangle$ peak which is further away from the wall at y^+=47 (y/H=0.15) with an estimated accuracy of 0.24 pixels. This shortcoming of PIV is fulfilled using micro-PTV, which provides measurement with higher spatial resolution and independent of the wall reflection. The slope of the mean velocity profile obtained from micro-PTV measurement within $2<y^+<5$ agrees with the Blasius law for the wall shear stress of smooth ducts. It also shows 6.1% reduction of wall shear stress over trapezoidal riblets with $s^+ = 11$, $h / s = 0.5$ and $\alpha = 30^\circ$. The extrapolation of the virtual origin over the riblet surface was also applied to estimate the virtual origin. Micro-PTV overestimated $\langle u^2 \rangle$ by 12% over the smooth wall. However, it was able to accurately measure the peak location of $\langle u^2 \rangle$ and its reduction over the riblet surface.

Measurement of $\langle uv \rangle$ using PIV in the center of the channel can be used to also estimate the wall shear stress. The intercept of a linear fit on $\langle uv \rangle$ profile within $0.2 < y / H < 0.5$ region was used to estimate the wall shear stress, showing 7.4% DR over the riblet surface.

3D-PTV showed a 9.4% reduction of $\langle w^2 \rangle$ peak over the riblet surface with estimated random noise error of about 0.34 pixels. Quadrant analysis of u and v fluctuations from PIV data shows attenuation of ejection and sweep motions while quadrant analysis of v and w from 3D-PTV depicted attenuation of v and w fluctuations over the riblet surface. The attenuation of the fluctuating components is an indication of weaker quasi-streamwise vortices over the riblet surfaces. The attenuations of the turbulence intensities above the riblets are observed to be 5.9%, 9.4% and 9.4% for the streamwise, wall-normal and spanwise component, respectively.

Three components of vorticity over the riblet surface obtained by tomo-PIV show negligible variation with respect to those over the smooth surface. The discrepancy is associated with the lack of spatial resolution and large measurement errors in the calculation of the velocity gradients. The estimated uncertainty of velocity gradients using the standard deviation of the divergence of the velocity field is 0.04 voxel/voxel in tomo-PIV data.

Spatial correlation of the velocity field in the streamwise direction indicates a larger streamwise length-scale over the riblet surface at $y^+ = 11$ while the difference diminishes further away from the wall at $y^+ = 25$. Therefore, a more organized arrangement of high and low speed streaks over the riblets wall is expected.

Acknowledgement

This work has been partially supported by the Natural Sciences and Engineering Research Council of Canada (NSERC RGPIN 1512 GHAEMI).

References

[1] T. Tsukahara, Y. Seki, H. Kawamura, and D. Tochio, "DNS of turbulent channel flow at very low Reynolds numbers," in *International symposium on turbulence and shear flow phenomena (TSFP-4)*, 2005, pp. 935–940.

[2] M. J. Walsh, "Riblets as a Viscous Drag Reduction Technique," *AIAA J.*, vol. 21, no. 4, pp. 485–486, Apr. 1983.

[3] M. Walsh and A. Lindemann, "Optimization and application of riblets for turbulent drag reduction," in *22nd Aerospace Sciences Meeting*, 1984, pp. 1–10.

[4] D. W. Bechert, M. Bruse, W. Hage, J. G. T. Van Der Hoeven, and G. Hoppe, "Experiments on drag-reducing surfaces and their optimization with an adjustable geometry," *J. Fluid Mech.*, vol. 338, pp. 59–87, May 1997.

[5] M. J. Walsh, "Drag characteristics of V-groove and transverse curvature riblets," in *Symposium on Viscous flow drag reduction*, 1979, pp. 168–184.

[6] R. Garcia-Mayoral and J. Jimenez, "Drag reduction by riblets," *Philos. Trans. R. Soc. A Math. Phys. Eng. Sci.*, vol. 369, no. 1940, pp. 1412–1427, Apr. 2011.

[7] J. Jimenez, "Turbulent flows over rough walls," *Annu. Rev. Fluid Mech.*, vol. 36, no. 1, pp. 173–196, Jan. 2004.

[8] S. K. Robinson, "Coherent Motions in the Turbulent Boundary Layer," *Annu. Rev. Fluid Mech.*, vol. 23, no. 1, pp. 601–639, Jan. 1991.

[9] H. Choi, P. Moin, and J. Kim, "Direct numerical simulation of turbulent flow over riblets," *J. Fluid Mech.*, vol. 255, pp. 503–539, Oct. 1993.

[10] Y. Suzuki and N. Kasagi, "Turbulent drag reduction mechanism above a riblet surface," *AIAA J.*, vol. 32, no. 9, pp. 1781–1790, Sep. 1994.

[11] S. J. Lee and S. H. Lee, "Flow field analysis of a turbulent boundary layer over a riblet surface," *Exp. Fluids*, vol. 30, no. 2, pp. 153–166, Feb. 2001.

[12] D. Goldstein, R. Handler, and L. Sirovich, "Direct numerical simulation of turbulent flow over a modeled riblet covered surface," *J. Fluid Mech.*, vol. 302, pp. 333–376, Nov. 1995.

[13] O. A. El-Samni, H. H. Chun, and H. S. Yoon, "Drag reduction of turbulent flow over thin rectangular riblets," *Int. J. Eng. Sci.*, vol. 45, no. 2–8, pp. 436–454, Feb. 2007.

[14] H. Chen, F. Rao, X. Shang, D. Zhang, and I. Hagiwara, "Flow over bio-inspired 3D herringbone wall riblets," *Exp. Fluids*, vol. 55, no.

3, p. 1698, Mar. 2014.

[15] M. Sasamori, H. Mamori, K. Iwamoto, and A. Murata, “Experimental study on drag-reduction effect due to sinusoidal riblets in turbulent channel flow,” *Exp. Fluids*, vol. 55, no. 10, p. 1828, Oct. 2014.

[16] K. Choi, “Near-wall structure of a turbulent boundary layer with riblets,” *J. Fluid Mech.*, vol. 208, pp. 417–458, Nov. 1989.

[17] S. Lee and Y. Choi, “Decrement of spanwise vortices by a drag-reducing riblet surface,” *J. Turbul.*, vol. 9, no. April 2013, pp. 1–15, 2008.

[18] R. B. Dean, “Reynolds Number Dependence of Skin Friction and Other Bulk Flow Variables in Two-Dimensional Rectangular Duct Flow,” *J. Fluids Eng.*, vol. 100, no. 2, pp. 215–223, 1978.

[19] L. Duan and M. Choudhari, “Effects of Riblets on Skin Friction and Heat Transfer in High-Speed Turbulent Boundary Layers,” in *50th AIAA Aerospace Sciences Meeting including the New Horizons Forum and Aerospace Exposition*, 2012, pp. 1–15.

[20] A. Hooshmand, R. Youngs, J. M. Wallace, and J. L. Balint, “An experimental study of changes in the structure of a turbulent boundary layer due to surface geometry changes,” in *21st Aerospace Sciences Meeting*, 1983, p. 230.

[21] D. W. Bechert and M. Bartenwerfer, “The viscous flow on surfaces with longitudinal ribs,” *J. Fluid Mech.*, vol. 206, pp. 105–129, Sep. 1989.

[22] R. Grüneberger and W. Hage, “Drag characteristics of longitudinal and transverse riblets at low dimensionless spacings,” *Exp. Fluids*, vol. 50, no. 2, pp. 363–373, Feb. 2011.

[23] C. D. Meinhart, S. T. Wereley, and J. G. Santiago, “A PIV Algorithm for Estimating Time-Averaged Velocity Fields,” *J. Fluids Eng.*, vol. 122, no. 2, pp. 285–289, 2000.

[24] J. Westerweel and F. Scarano, “Universal outlier detection for PIV data,” *Exp. Fluids*, vol. 39, no. 6, pp. 1096–1100, Dec. 2005.

[25] Navitar, “12X Zoom Performance Specifications | Navitar,” 2016. [Online]. Available: https://navitar.com/products/imaging-optics/high-magnification-imaging/12x-zoom/.

[26] I. T. Young, R. Zagers, L. J. van Vliet, J. Mullikin, F. Boddeke, and H. Netten, “Depth-of-focus in microscopy,” in *Proceedings of the 8th Scandinavian conference on image analysis*, 1993, pp. 493–498.

[27] C. J. Kähler, S. Scharnowski, and C. Cierpka, “On the uncertainty of digital PIV and PTV near walls,” *Exp. Fluids*, vol. 52, no. 6, pp. 1641–1656, Jun. 2012.

[28] B. Wieneke, “Volume self-calibration for 3D particle image velocimetry,” *Exp. Fluids*, vol. 45, no. 4, pp. 549–556, Oct. 2008.

[29] F. Scarano and C. Poelma, “Three-dimensional vorticity patterns of cylinder wakes,” *Exp. Fluids*, vol. 47, pp. 69–83, 2009.

[30] S. Park and J. M. Wallace, “Flow alteration and drag reduction by riblets in a turbulent boundary layer,” *AIAA J.*, vol. 32, no. 1, pp. 31–38, Jan. 1994.

[31] D. Roggenkamp, W. Li, P. Meysonnat, M. Klaas, and W. Schröder, “Experimental Analysis of Turbulent Friction Drag Reduction Due To Spanwise Transversal Surface Waves,” in *International symposium on turbulence and shear flow phenomena (TSFP-9)*, 2015.

[32] N. Kasagi, Y. Sumitani, Y. Suzuki, and O. Iida, “Kinematics of the quasi-coherent vortical structure in near-wall turbulence,” *Int. J. Heat Fluid Flow*, vol. 16, no. 1, pp. 2–10, Feb. 1995.

[33] W. W. Willmarth and S. S. Lu, “Structure of the Reynolds stress near the wall,” *J. Fluid Mech.*, vol. 55, no. 1, pp. 65–92, Sep. 1972.

[34] J. M. Wallace, H. Eckelmann, and R. S. Brodkey, “The wall region in turbulent shear flow,” *J. Fluid Mech.*, vol. 54, no. 1, pp. 39–48, Jul. 1972.

[35] J. Kim, P. Moin, and R. Moser, “Turbulence statistics in fully developed channel flow at low Reynolds number,” *J. Fluid Mech.*, vol. 177, pp. 133–166, 1987.

[36] G. E. Elsinga, R. J. Adrian, B. W. Van Oudheusden, and F. Scarano, “Three-dimensional vortex organization in a high-Reynolds-number supersonic turbulent boundary layer,” *J. Fluid Mech.*, vol. 644, pp. 35–60, Feb. 2010.

[37] N. A. Worth, T. B. Nickels, and N. Swaminathan, “A tomographic PIV resolution study based on homogeneous isotropic turbulence DNS data,” *Exp. Fluids*, vol. 49, no. 3, pp. 637–656, Sep. 2010.

[38] C. M. White, V. S. R. Somandepalli, and M. G. Mungal, “The turbulence structure of drag-reduced boundary layer flow,” *Exp. Fluids*, vol. 36, no. 1, pp. 62–69, Jan. 2004.